

On the local properties of highly nonlinear unsteady gravity water waves. Part 2. Dynamics and onset of breaking

X. Barthelemy^{1,2} †, M.L. Banner¹, W.L. Peirson²,
 F. Fedele³, M. Allis² and F. Dias⁴

¹School of Mathematics and Statistics, UNSW Australia, Sydney NSW 2052, Australia

²Water Research Laboratory, School of Civil and Environmental Engineering, UNSW Australia, Sydney NSW 2052, Australia

³School of Civil and Environmental Engineering, and School of Electrical and Computer Engineering, Georgia Institute of Technology, Atlanta, GA 30332, USA.

⁴UCD School of Mathematical Sciences, University College Dublin, Belfield, Dublin 4, Ireland

(Received ?; revised ?; accepted ?. - To be entered by editorial office)

We revisit the classical, but as yet unresolved problem of predicting the breaking onset of 2D and 3D irrotational gravity water waves. This study focuses on domains with flat bottom topography and conditions ranging from deep to intermediate depth (depth to wavelength ratio between 1 and 0.2). Using a fully-nonlinear boundary element model, our initial calculations investigated geometric, kinematic and energetic differences between maximally recurrent and marginally breaking waves in focusing wave groups. Maximally-recurrent waves are clearly separated from marginally-breaking waves by their energy fluxes localized near the crest region. Specifically, tracking the local ratio of energy flux velocity to crest speed at the crest of the tallest wave in the evolving group provides a robust breaking onset threshold parameter. Warning of imminent breaking onset was found to depend on the strength of breaking, but was detectable only up to half a carrier wave period prior to a breaking event.

Key words: Authors should not enter keywords on the manuscript, as these must be chosen by the author during the online submission process and will then be added during the typesetting process (see <http://journals.cambridge.org/data/relatedlink/jfm-keywords.pdf> for the full list)

1. Introduction

In the open ocean, wave breaking is a familiar but poorly understood phenomenon, both of the dominant waves and also of the superimposed directional distribution of shorter waves. The physics of the breaking process, as well as predicting its onset and strength are of fundamental importance in quantifying atmosphere-ocean exchanges, determining structural loadings on ships and platforms and optimising operational strategies for a number of maritime enterprises.

Many criteria for predicting breaking onset of deep-water waves have been proposed in the literature since the pioneering study of Stokes (1847). These criteria have been derived from theoretical arguments based on idealized models, numerical simulations, laboratory experiments and field observations. They have mostly avoided addressing the

† Email address for correspondence: x.barthelemy@wrl.unsw.edu.au

elusive underlying dynamical processes. In any event, these approaches have largely failed to yield a robust breaking threshold for phase-resolved waves in the physical domain. This has delayed the development of a reliable predictive capability for wave breaking in the spectral domain, needed to underpin the spectral dissipation source term used in present operational wave model forecasts.

It has long been considered that breaking is a thresholded process, with criteria for predicting breaking onset falling into three categories: geometric, kinematic and energetic. The majority of proposed breaking criteria have been based on a geometric or kinematic threshold, and mainly limited to plane (2D) waves. Geometric threshold variables have included wave steepness, wave asymmetry, and maximum theoretical (global) steepness; kinematic threshold variables have included Lagrangian crest acceleration, crest speed/phase speed ratio, among others. The recent comprehensive review article by Perlin *et al.* (2013) provides an excellent detailed overview of the collective observational and theoretical effort and outcomes based on kinematic/geometric approaches. Shemer (2013) adds to their otherwise exhaustive coverage. Overall, the current consensus is that geometric/kinematic thresholds do not robustly predict deep water wave breaking onset.

A third path has been explored to explain the onset of breaking, so-called dynamical criteria. Tulin & Li (1992), Song & Banner (2002), Tian *et al.* (2008) made significant contributions to this approach which explores the existence of an energy flux threshold linked to the physics of breaking onset. This concept relies on the dynamical evolution of the intra-group energy flux which causes the tallest crest of an unsteady wave group structure to break when a local stability threshold is exceeded. Monitoring these complex quantities in a highly nonlinear, spatially non-uniform and unsteady framework makes rigorous analysis very difficult, for which a first step has been made for 2D waves by Tulin & Li (1992). Complementary insights came from a numerical simulation study, further developed by Wang *et al.* (1993) and Wang *et al.* (1995). Schultz *et al.* (1994) reported a criteria based on the (potential) energy transfer rate which induces breaking onset when the potential energy exceeds 52% of the total energy. Later, Banner & Tian (1998), Song & Banner (2002) and the complementary experimental study of Banner & Peirson (2007) investigated a growth rate based on a parametric energy convergence rate for 2D wave groups, using a frame of reference that tracks the wave group maximum. Perlin *et al.* (2013) discuss the merits and validation of this approach based on the further study of Tian *et al.* (2008) for 2D wave breaking. In the present study, we revisited this approach in the context of our 2D and 3D simulations, for which our findings are summarised in section 4.2 below.

Finally, we mention that there are very significant additional challenges in representing wave breaking in broad-banded directional sea states in the spectral (wavenumber-frequency) context. This is the domain used for computing ocean wave model forecasts (e.g. see Chalikov & Babanin (2012)). In that context, there is even less consensus on how to predict/identify breaking events. However, this is beyond the scope of the present paper, where we focus attention on wave breaking in the physical space-time domain. Our assessment of the present status of this topic is that a robust understanding of breaking onset remains elusive, which has precluded its reliable prediction even in controlled laboratory and numerical wave basin conditions. Here, we describe our investigation which addresses this time-honoured knowledge gap in the context of discovering a unified breaking criterion valid for 2D and 3D gravity water waves propagating over flat topography, for water depths ranging from intermediate (20% of the wavelength) to deep (one wavelength).

2. Methodology

This study utilises the same approach, numerical methodology and datasets as described in detail in Barthelemy *et al.* (2015). These data have been produced by a numerical wave tank, WSIM, initially developed by Grilli *et al.* (1989) and used in multiple topics related to wave propagation and wave breaking (see chapter 3 of Ma (2010)). It has been validated extensively using analytical test cases and also in previous studies.

WSIM uses a Boundary Element Method (BEM) to compute field variables. The 16-node quadrilateral elements provide a global order three precision, and high-order tangential derivatives necessary for the time discretisation are computed in a local curvilinear coordinate system giving a fourth order precision. A fast PTMA scheme has been used to inverse the BEM problem.

Simulations were run using multiple resolutions, from 8 points per wavelength in medium resolution up to 16 points per wavelength in high resolution. The number of points in the transverse (y) direction or in the depth (z) is adjusted to keep the boundary element aspect ratio close to 1.

The mixed Eulerian-Lagrangian numerical scheme and the high nonlinearity of the wave groups generated make the free surface mesh susceptible to distortion by the Lagrangian drift current. Precautions were taken so even at maximum recurrence, only a moderate Lagrangian drift was produced and the mesh did not deform significantly.

The results are represented using a deep water non-dimensional scaling. The reference length is the wavelength λ_p and the time scale is based on the paddle signal driving frequency ω_p . The deep water dispersion relation imposes a gravitational acceleration of $g_{DW} = 2\pi$ and a reference linear phase speed $c_{DW} = 1$. The dataset has been produced using a ratio depth to wavelength within a range of $0.2 < \frac{d}{\lambda_p} < 1$.

Wave groups were produced using a bottom-hinged flap snake wave-maker paddle at one end of the tank, giving the capacity to produce 2D and 3D wave packets. Shallow water waves were generated in the same manner to keep consistency between the different runs with the same wave class and different depths.

The wave groups were generated by driving the wavemaker with a motion $x_p(t, y)$ at the still water level, using the prescribed 'chirp' motion from Song & Banner (2002). The following expression defines Class 3 waves, N being the number of waves, ω_p the paddle frequency, $\theta(t) = k[x_w - ct] - \theta_0$ the phase and C_{t2} the frequency chirp rate:

$$X_p(t) = \left(1 + \tanh \left(\frac{4\omega_p t}{N\pi} \right) \right) \left(1 - \tanh \left(\frac{4(\omega_p t - 2N\pi)}{N\pi} \right) \right) \quad (2.1)$$

$$\sin \left(\omega_p \left(t - \frac{\omega_p C_{t2} t^2}{2} \right) + \Phi(X_{conv}, Y_{conv}) \right). \quad (2.2)$$

A time delay were introduced to ensure any initial paddle oscillations are of the order of the double-precision zero. If 3D waves are to be produced by the snake paddle, the phase Φ becomes a function of (X_{conv}, Y_{conv}) which specify the linear convergence point coordinates, as defined by Dalrymple & Kirby (1988) and Dalrymple (1989):

$$\theta_n = \arctan \frac{y - Y_{conv}}{X_{conv}} \quad (2.3)$$

$$\Phi = k \cdot y \cdot \sin \theta_n + k (X_{conv} \cos \theta_n + Y_{conv} \sin \theta_n) \quad (2.4)$$

The far end of the NWT from the wave generator has a fully-absorbing boundary condition, as in Grilli & Horrillo (1997).

3. Analysis of our simulation data using previous breaking criteria

The recent review paper of Perlin *et al.* (2013) provides a detailed analysis of the different classes of proposed breaking criteria. Shortcomings have been identified in each of the criteria proposed to date. For the record, several of these breaking criteria were applied to our simulation data and their validity evaluated.

3.1. Geometrical criteria

As reported in Perlin *et al.* (2013), geometric threshold criteria were not found to be robust (in the generic sense) in previous observational studies. Figure 3 provides an overview of the performance of the steepness criterion for breaking onset for the present data set. The results shown confirm the previous findings that breaking waves cannot be separated from non-breaking waves with a seemingly obvious parameter such as the wave crest steepness. This figure shows the steepness of each local crest maximum in an ensemble of evolving wave groups. Circles represent recurrent wave groups and stars represent breaking crests, plotted against the local crest steepness S_c as defined in Banner *et al.* (2014). It is seen that breaking onset cannot be discriminated by the steepness criterion because some breaking crest cases have a significantly lower steepness than recurrent waves.

3.2. Kinematic criteria

Various kinematic threshold variables have been proposed as the basis of potential generic breaking criteria, as described in Perlin *et al.* (2013). They have included Lagrangian crest acceleration, crest speed to phase speed ratio, crest speed to group speed ratio, amongst others. In Banner *et al.* (2014), the influence of unsteadiness in highly nonlinear wave packets was investigated using numerical simulations and complementary laboratory and ocean tower measurements. That study highlights the existence of a significant kinematic/geometric phenomenon attributable to the larger degrees of freedom available. The result is an additional generic oscillatory crest leaning mode that characterises the carrier wave evolution. This leads to a systematic crest speed slowdown of $\approx 20\%$ of the linear phase velocity, and reconciles why breaking crests are observed to have initial speeds $\approx 20\%$ lower than linear theory predicts for that wavelength. While the crest slowdown is not fully understood, it is the underlying condition from which breaking onset initiates. While Stansell & MacFarlane (2002) and Kurnia & van Groesen (2014) mention a variety of purely kinematic criteria (ratio of fluid velocity to wave speed larger than 0.7, 0.8 and 1) close to our findings in this present paper, there is no guidance to the universality of the detection of the breaking onset.

3.3. Dynamical criteria

Dynamical criteria link the physics of breaking onset to the energy fluxes associated with the underlying unsteady wave group structure. The basic idea suggests that the exchange of intra-group energy fluxes exceeding a local stability level at the tallest crest triggers this crest to break. The highly nonlinear, spatially non-uniform and unsteady nature of the flow field makes rigorous analysis very difficult. Tulin & Li (1992) made interesting inroads with their 2D intra-group energy flux analysis and subsequent complementary numerical simulation studies of Wang *et al.* (1993) and Wang *et al.* (1995) concluded that breaking onset is initiated when $u/c_g > 1$, where u is the particle velocity and c_g is the linear group speed. This prediction is in marked contrast with the traditional kinematic criterion $u/c_p > 1$, where c_p is the linear phase speed. As described in section 1, Song & Banner (2002) (and subsequently Banner & Peirson (2007)) investigated a parametric energy convergence rate for 2D wave groups following the wave group maximum,

which Perlin *et al.* (2013) discusses in detail. In our present study, we found that 3D breaking onset did not conform closely to the 2D threshold growth rate proposed by Song & Banner (2002). We noted that the computed local carrier wavenumber used in this growth rate (in 2D cases, as well as in 3D cases) did not increase progressively as the wave steepened, as was assumed in the 2D study of Song & Banner (2002), thereby degrading the diagnostic growth rate trajectory. We also noted the need to compute the evolution for the duration of a finite number (at least 3) of local crest maxima in order to be able to establish the diagnostic growth rate. This diminished the utility of this approach especially for cases when the wave breaking onset develops very rapidly. This motivated seeking a more direct breaking criterion based on an energy flux threshold.

4. New breaking criterion based on the local energy flux velocity

Conceptually, the onset of breaking can be regarded as the inability of the waveform to accommodate an excess local wave energy flux. It is observed that breaking events typically occur at the tallest crests of gravity waves within groups, showing the preferred localisation of the phenomenon. Excess local wave energy flux can arise from a variety of sources, such as intra-wave energy exchanges, wind-wave exchange, geometrical and temporal 3D wave focusing, wave-current interactions, among others. For the present focus on unforced water wave groups, we hypothesise that the same breaking onset physics should apply whether the wave group is evolving in deep water or in shallow water. This is the premise underlying our pursuit of a generic breaking criterion. After multiple tests and the shortcomings of the various criteria described above, our attention focused on the role of excess wave energy flux as the underpinning element. The wave energy flux vector is defined and discussed in Phillips (1977) (equation (2.3.2)), together with a detailed discussion of its conservation equation (3.6.14).

4.1. Energy flux in nonlinear wave groups.

Phillips (1977) defines the local energy flux vector

$$\mathbf{F} = \mathbf{U} \left(P + \rho g z + \frac{1}{2} \rho \mathbf{U}^2 \right) = \mathbf{U} \left(-\frac{\partial \phi}{\partial t} + C(t) \right) \quad (4.1)$$

where $C(t)$ is the Bernoulli constant, the magnitude of \mathbf{F} is $\|\mathbf{F}\|$ and the local energy density is given by $E = \rho g z + \frac{1}{2} \rho \mathbf{U}^2$.

With the above definitions, Phillips (1977) (3.6.14) derives the conservation law for the depth-integrated energy in the form:

$$\frac{\partial}{\partial t} \int_{depth} E + \frac{\partial}{\partial x_\alpha} \int_{depth} F_\alpha = 0 \quad (4.2)$$

where $a = 1, 2$ represent the (x, y) horizontal directions. Phillips' inference that the depth-integrated vertical (z) component of the gradient of the flux vanishes can be easily verified using the boundary conditions:

$$\frac{\partial}{\partial z} \int_{depth} F_z dz = 0. \quad (4.3)$$

We performed an analysis of the local behaviour of the depth-integrated energy, energy flux and its gradient at maximal focusing for representative nonlinear wave packets. These cases share the same characteristics and belong to the C3N5 family, a Class 3 chirped wave packet initially with five waves in the temporal packet. Our aim was to determine whether

breaking onset presented a distinctive signature in the depth-integrated energy context. The detailed analysis, presented in Appendix A, highlights the very interesting conclusion that if only the depth-integrated energy field is tracked, the onset of breaking does not stand out conspicuously. To detect the transition to breaking above the background wave energy, a local analysis of the energy fluxes is needed. This is described in the following section.

4.2. *Breaking criterion based on the local energy flux velocity*

The ratio of the local energy flux vector \mathbf{F} and the local energy density E can now be formed, and define a measure of the relative strength of the energy flux. This ratio \mathbf{F}/E has the dimension of a velocity, and can be considered as a local energy transport velocity. When integrated over the whole wave group, this velocity becomes the familiar group velocity.

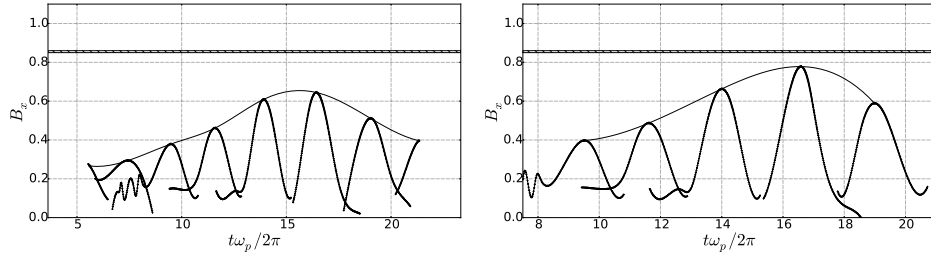
A recent investigation by Banner *et al.* (2014) and Barthelemy *et al.* (2015) provides new insights into underlying wave group behaviour. It explores the consequences of relaxing the steadiness constraint in classical periodic wave train theory. Specifically, every wave in an unsteady wave group experiences a dynamic leaning cycle. Crests and troughs enter at the rear of the wave group first leaning forward, then transitioning through symmetry and subsequently leaning backward as they propagate towards the front of the wave group. This leaning cycle creates a generic crest slowdown to around 80% of the peak spectral velocity c_0 , with a weak dependence on the (local) steepness of the crest or trough. Figure 9 in Barthelemy *et al.* (2015) shows the velocity of a wave crest breaking at its highest steepness. Breaking onset commences when the crest is moving very close to its slowest speed, and therefore the breaking crest "whitecap" commences at a significantly lower initial velocity than expected.

The idea of comparing the local energy flux speed with the local crest speed follows naturally from these observations. During the crest propagation, the local energy flux speed becomes maximal near the tip of the crest. We can now define the ratio of the previously defined vectorial quantity \mathbf{F}/E and the local crest velocity \mathbf{c} . Because the energy flux \mathbf{F} and the crest velocity \mathbf{c} are vectors, a projection along the wave propagation direction (taken as the x direction) can be made using F_x and c_x , the respective projections on the x -axis of \mathbf{F} and \mathbf{c} , and this ratio creates a non-dimensional parameter $B_x = F_x/Ec_x$. Its potential as an energy flux-based breaking criterion parameter that takes into account the wave dynamics directly is now explored. This local quantity is defined everywhere in the flow domain, including crests and troughs. When breaking onset occurs, the B_x distribution provides a useful visualisation of the evolving subsurface distribution of excess wave energy flux.

Another choice could be made using the norm of the local energy flux vector, but to be consistent, the B parameter would need to be constructed using the full 3D crest velocity, including the lateral and vertical velocity components using $F = \|\mathbf{F}\|$ in the previously defined quantity \mathbf{F}/E , i.e. F/E , and the local crest velocity $c = \|\mathbf{c}\|$. However, this makes no difference when the crest reaches its maximum, as the vertical component vanishes and likewise the respective energy flux component, as shown in Appendix A.1.

4.2.1. *Manifestation at the surface*

At the free surface, the pressure P that appears in the energy flux vector \mathbf{F} is constant, and can be taken as zero without loss of generality (e.g. see Lamb (1945), §18, 20). This results in a very convenient simplification. The energy flux velocity reduces to the particle velocity (collinear with the crest velocity) and our dynamic breaking criterion based on excess energy flux reduces to a kinematic criterion at the free surface:



(a) Breaking criterion B_x plotted against time for a recurrent Class 3 N9 wave group with a generating paddle amplitude $A=0.46$
(b) Breaking criterion B_x plotted against time for a maximum recurrent Class 3 N9 wave group with a generating paddle amplitude $A=0.47$

Figure 1: Breaking criterion B_x plotted against time for recurrent cases of the Class 3 N9 family

$$F_x/Ec_x < \text{threshold} \quad (4.4)$$

It is shown in Appendix A.1 that $F = F_x$ at crest maximum (with or without breaking), and also naturally $c = c_x$, which implies $B = B_x$ at the crest.

The various numerical experiments shown in Table 1 suggest the newly proposed criterion provides a uniform breaking onset threshold across focusing 2D and 3D wave groups evolving over flat bottom topography in water depths (d) spanning intermediate to deep ($0.2 < d/\lambda_p < 1$). We note that the energy flux is a vector quantity and our criterion is able to accommodate the lateral energy flux in 3D converging cases.

The onset of breaking was found to occur when $0.85 < B_x < 0.86$. After factoring in the reduced crest speed of $\approx 0.8c_0$, we note that this corresponds to $u/c_0 \approx 0.7$, which is well below the often-quoted classical kinematic breaking criterion $u/c_0 > 1$. This robust threshold is found to hold for our entire ensemble of numerical experiments addressing 2D and 3D deep-water and intermediate-depth cases. For any growing crest, when B_x exceeds the threshold, the crest always evolves to break. To our knowledge, this breaking criterion unifies, for the first time, both 2D and 3D breaking onset for deep to intermediate-depth water waves propagating over flat bottom topography. It remains for the future to validate that this criterion extends to shallower water waves ($d/\lambda_p < 0.2$) on flat topography and waves shoaling on inclined bottom topography.

Two examples of this behaviour are described in detail below. Figures 1b and 2a show the time evolution of the breaking parameter B_x following the crest maximum during the group propagation. The two cases shown are maximum recurrence and incipient breaking C3N9 2D deep-water case. The hatched zone is the identified threshold level of $0.85 - 0.86$ above which crests will proceed to break. The symbols allow tracking the trajectories for each crest in the wave group during its evolution. In the marginal recurrence case (Figure 1b), the trajectories never cross the hatched zone, in contrast with Figure 2a, which shows the marginal breaking case of the same wave group class. In this case, the trajectory of the breaking crest (shown in black) clearly crosses the threshold.

In these examples, a computed spline passing through all the local crest maxima shows their longer-term evolution trajectory. In the breaking case, the spline crosses the hatched breaking threshold zone before breaking subsequently initiates, providing an advance warning of up to half a carrier wave period. This behaviour is representative of every breaking case investigated.

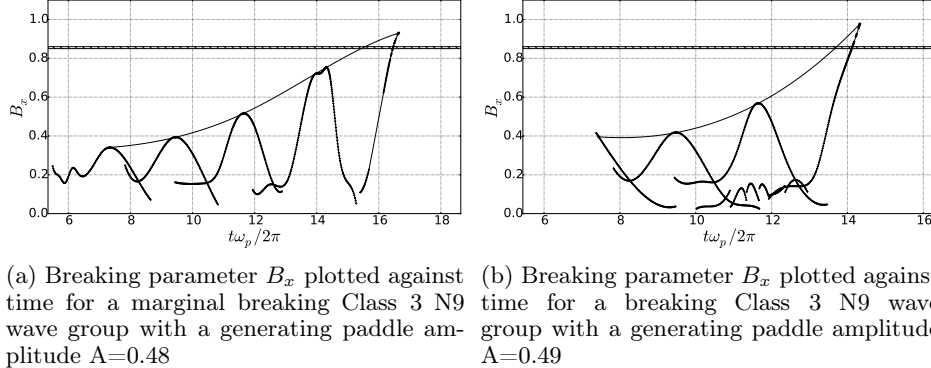


Figure 2: Breaking parameter B_x plotted against time for breaking cases of the Class 3 N9 family

Figure 3 shows a compilation of every value of the breaking onset parameter B_x against the corresponding crest steepness S_c computed in this study. It shows recurrent cases at their maximum height (open circles), and breaking crests at their onset. Both 2D and 3D deep and intermediate depth cases are included. In this figure, the vertical hatched zone on the right represents the classical Stokes local steepness limit expressed in terms of S_c rather than ak . The horizontal hatched zone $[0.85 < B_x < 0.86]$ is the breaking threshold determined from our ensemble of numerical simulations. This figure highlights two significant findings. The major finding of this study is the discovery of a clear separation between recurrent and breaking crests. For recurrence cases, our proposed breaking onset parameter B_x is always lower than 0.85, below which crests were never found to break, and higher than 0.86, when breaking was always found to occur. This identifies the breaking onset threshold zone for B_x as $[0.85, 0.86]$. The other finding apparent in this figure concerns the relationship between crest steepness at maximum wave height and breaking onset. Crest steepness is clearly not a threshold criterion that is able to discriminate between breaking and recurrence. This is evident as the local steepness for breaking crests can be lower than the local steepness of recurrent evolution cases for a given depth (or kd). We note that a straight line can be drawn between $(0, 0)$ and $(S_{k_{max}}, 0.855)$. All the circles appear closely aligned at low steepness and then a departure from this trend occurs, possibly due to nonlinearities, where the B_x parameter grows faster than the steepness. This transition occurs at higher steepness levels for intermediate-depth cases than for deep water cases. Remarkably, the limiting case for shallow water conditions ($kd \rightarrow 0$) appears to asymptote to the Stokes limiting steepness.

Table 1 summarises all the cases post-processed for the study, with their properties.

4.2.2. Subsurface energy flux considerations

The breaking parameter B is based on the local wave energy flux F normalised by the local wave energy density E and the wave crest speed c defined at the maximum elevation of the crest. B exists both on the surface and in the interior of the wave domain. It can be computed for maximum recurrent and crests evolving to break, up to the point of breaking onset. Figure 5 and Figure 6 present key properties of interest, respectively, of 3D and 2D waves evolving towards breaking onset. Each of these figures represent two snapshots (A and B) at different stages of development of the wave field. Each snapshot shows two different aspects.

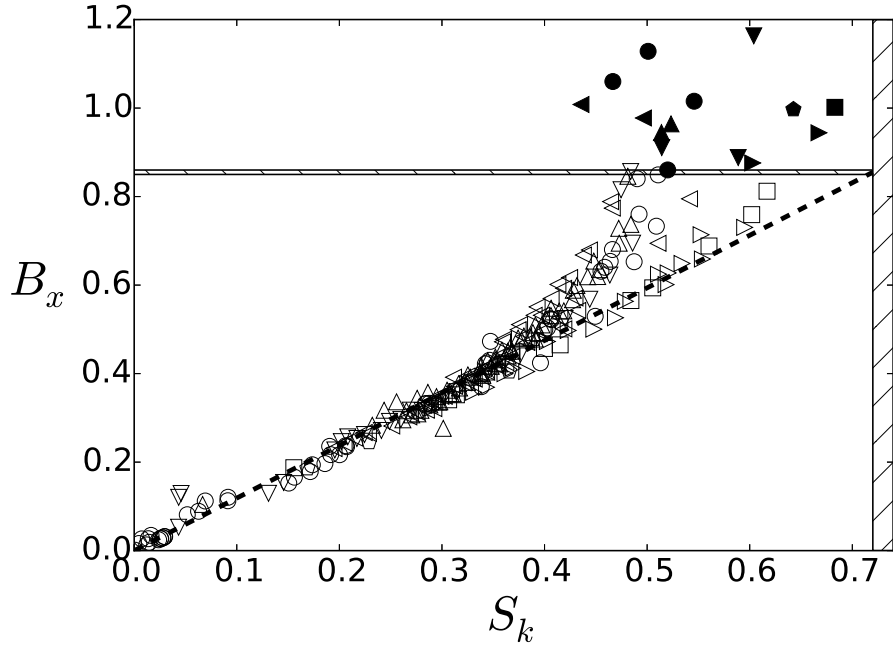


Figure 3: Breaking parameter B_x plotted against local steepness S_k . The horizontal hatched zone at $0.85 < B_x < 0.86$ is the threshold which partitions breaking from non-breaking cases; the vertical hatched zone $S_c > 0.72$ is the deep water Stokes limit. Hollow symbols represent recurrent crests and filled symbols represent breaking crests. The symbols code the Class 3 wave group families as follow: circles: N5 2D deep water, downwards pointing triangles: N5 3D deep water, upwards pointing triangles: N7 2D deep water, leftwards pointing triangles: N9 2D deep water, rightwards pointing triangles: N9 2D $0.2 < d/\lambda_p < 1$, squares: N9 2D $d/\lambda_p = 0.2$, pentagons N9 3D $0.2 \leq d/\lambda_p < 1$.

The first is a color-coded representation showing contours of the x-component breaking onset parameter B_x on the crest surface (Figures 5a, 5b, 6a and 6b).

The other plot is a vertical plane slice on the symmetry axis of the crest, taken along the blue line shown in the surface plot (Figures 5c, 5d, 6c and 6d). These figures need the companion plots of the crest velocity history (Figure 4a and Figure 4b). The common colour code associated with the values of B_x , is as follows: red: $B_x > 0.85$; green: $0.7 < B_x < 0.85$; blue: $0.6 < B_x < 0.7$; yellow: $0.5 < B_x < 0.6$; magenta: $0.4 < B_x < 0.5$; white: $B_x < 0.4$.

These plots highlight the localisation of the maxima at the wave crests. The 2D and 3D cases are similar, as seen by the localisation of the maximum of the spatial distribution of B_x at the crest maximum. Of further interest is the spatial extent of the region involved in a breaking onset event. Based on the B_x parameter threshold, the horizontal extent of the zone where B_x values start to be significant is close to 10% of the wavelength, within the already narrow crest region.

We note that observational validation of our new breaking criterion is likely to be challenging, as it is localised within a rapidly-evolving, narrow zone. Its horizontal extent where B_x values exceed the breaking threshold is only about 3% of the wavelength, and since the non-dimensional wave speed is close to 0.8 at breaking, a fixed probe will reside

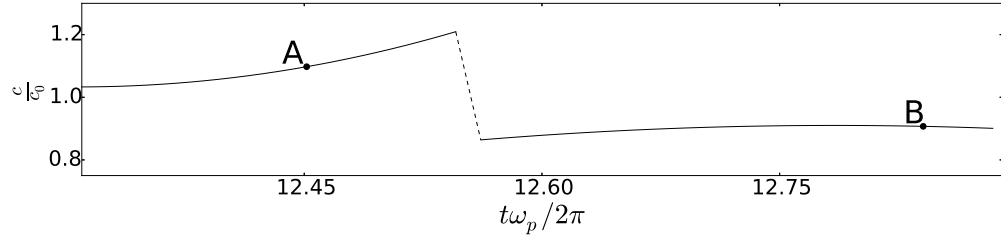
Name	S_c	Max	Breaking	B_x
C3N5A0.05	0.012	N	0.012	
C3N5A0.3	0.206	N	0.237	
C3N5A0.511	0.509	N	0.733	
C3N5A0.514	0.520	Y	0.860	
C3N5A0.516	0.545	Y	1.015	
C3N5A0.519	0.500	Y	1.128	
C3N5A0.519	0.466	Y	1.059	
C3N5A0.32X10	0.420	N	0.524	
C3N5A0.33X10	0.474	N	0.815	
C3N5A0.34X10	0.588	Y	0.888	
C3N5A0.35X10	0.603	Y	1.163	
C3N5A0.36X10	0.514	Y	0.910	
C3N7A0.41	0.344	N	0.429	
C3N7A0.42	0.358	N	0.452	
C3N7A0.43	0.374	N	0.480	
C3N7A0.44	0.391	N	0.509	
C3N7A0.45	0.406	N	0.547	
C3N7A0.46	0.428	N	0.588	
C3N7A0.47	0.448	N	0.654	
C3N7A0.48	0.484	N	0.737	
C3N7A0.49	0.513	Y	0.944	
C3N7A0.50	0.523	Y	0.964	
C3N9A0.42	0.360	N	0.477	
C3N9A0.43	0.375	N	0.510	
C3N9A0.45	0.413	N	0.601	
C3N9A0.46	0.437	N	0.667	
C3N9A0.47	0.464	N	0.788	
C3N9A0.48	0.496	Y	0.952	
C3N9A0.49	0.433	Y	0.977	
C3N9A0.44	0.392	N	0.550	
D0.4C3N9A1.05	0.616	N	0.812	
D0.4C3N9A1.07	0.682	Y	1.001	
D0.5C3N9A0.95	0.595	N	0.730	
D0.5C3N9A0.97	0.667	Y	0.944	
D0.5C3N9A0.55X10	0.642	Y	0.997	
D0.75C3N9A0.77	0.552	N	0.713	
D0.75C3N9A0.79	0.602	Y	0.875	
D1C3N9A0.65	0.541	N	0.794	

Table 1: Maximum B_x for each simulation case

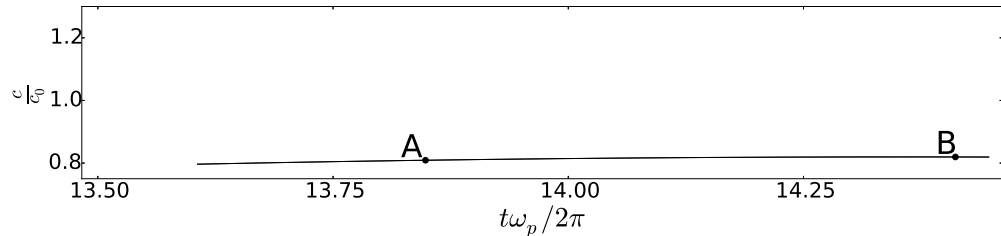
in this zone for only around 0.04 non-dimensional time units. Accurate determination of the rapidly evolving crest speed and its associated surface fluid speed is a demanding measurement.

The zones where B_x becomes appreciable in 2D and 3D breaking waves have approximately the same vertical extent, but the surface distribution of B_x differs considerably. For 3D converging waves, the maximal values are positioned on side lobes off the symmetry axis. These lobes then converge towards the symmetry axis, with B_x maximising on the symmetry axis where the wave breaks.

In contrast, 2D breaking waves have an almost constant spanwise distribution of B_x values, with a minor variations observed where the loci of maximum B_x values are on either side of the symmetry axis. This behaviour has been confirmed observationally for 2D breakers in Figures 5.2, 5.3 and 5.4 in Allis (2013) where the onset of 2D wave



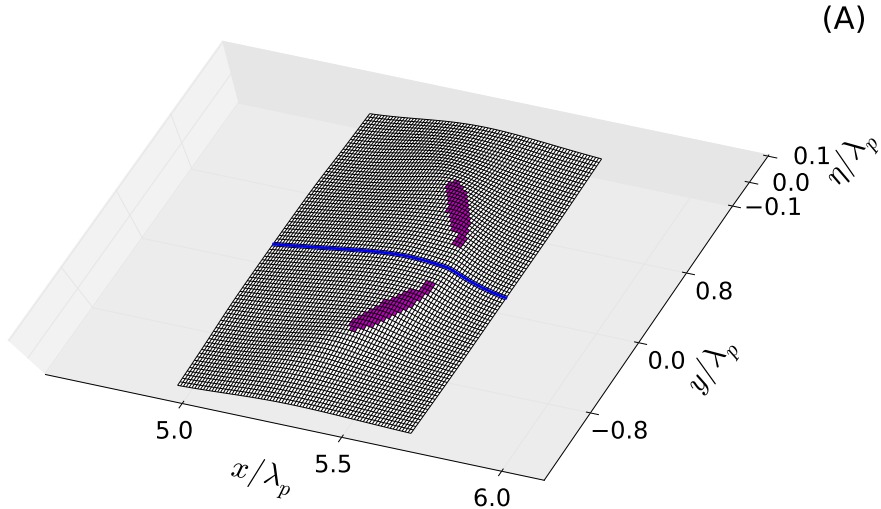
(a) Velocity history of the 3D C3N5A0.36 Breaking Case



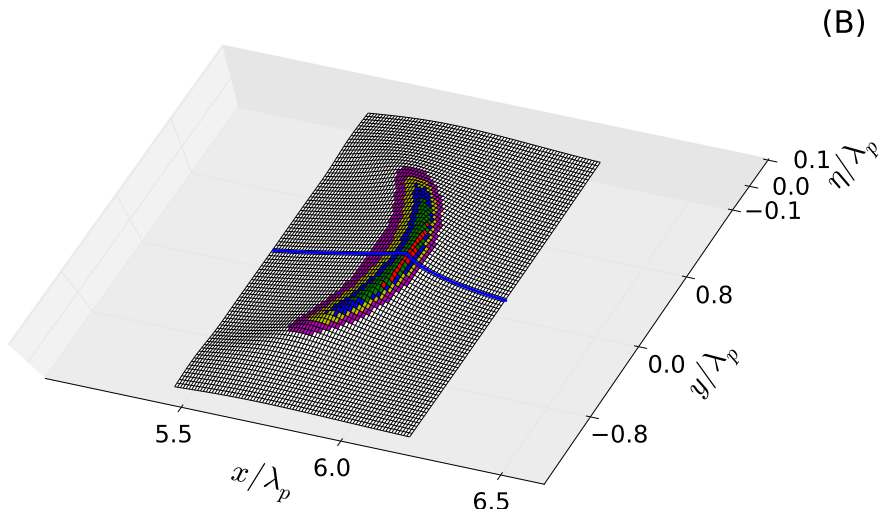
(b) Velocity history of the 2D C3N5A0.514 Breaking Case

Figure 4: Velocity history of the 3D C3N5A0.36 and the 2D C3N5A0.514 breaking cases of the figures 5 and 6

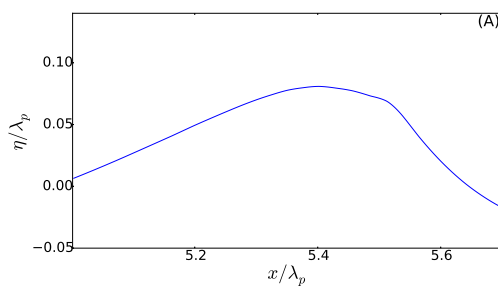
breaking in a wave basin was sometimes observed to occur at similar lateral positions on either side of the basin centreline.



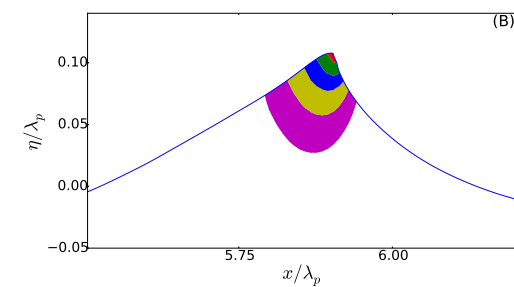
(a) Colour-coded zones of the breaking parameter B_x on the free surface at $t = 12.45$. The blue line is the location of the slice seen in 5c



(b) Colour-coded zones of the breaking parameter B_x on the free surface at $t = 12.84$. The blue line is the location of the slice seen in 5d

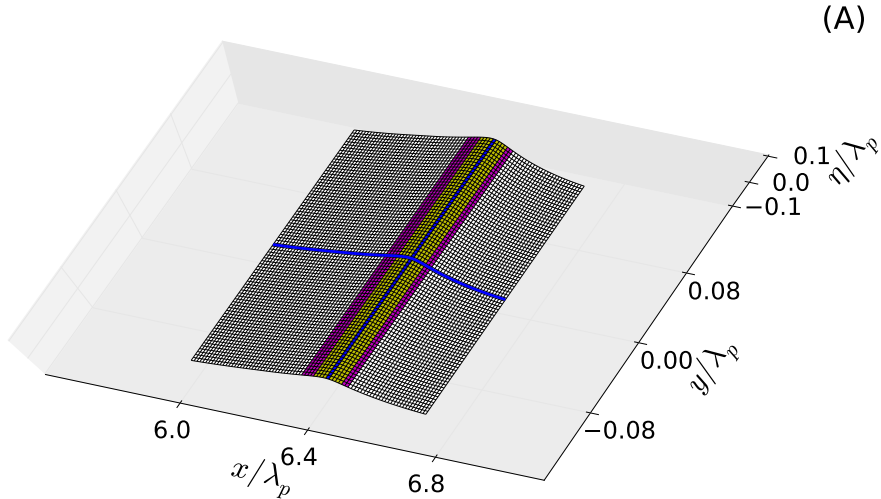


(c) Colour-coded cross-section within the slice $y = 0$ shown in figure 5a

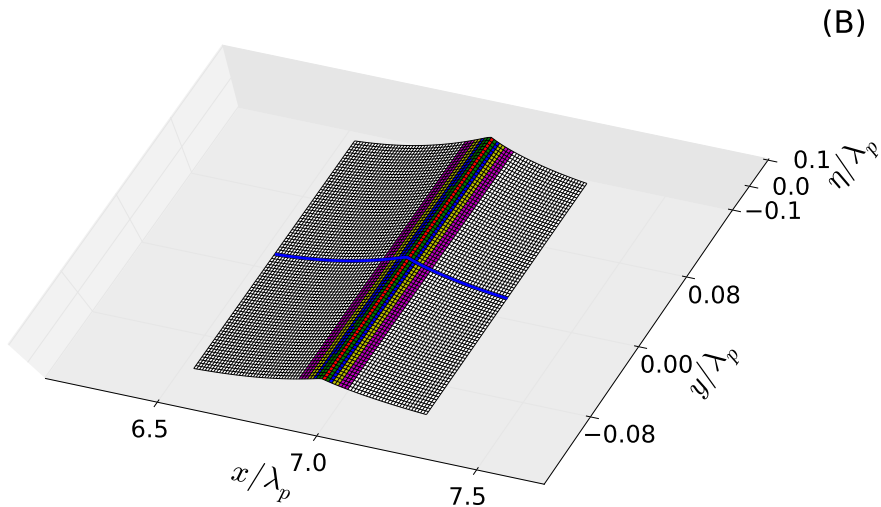


(d) Colour-coded cross-section within the slice $y = 0$ shown in figure 5b

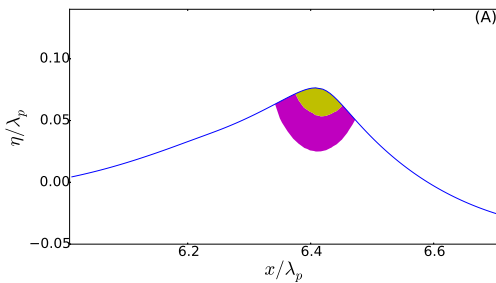
Figure 5: Contours of the breaking criterion B_x . The regions are colour-coded as follows: red: $B_x > 0.85$; green: $0.7 < B_x < 0.85$; blue: $0.6 < B_x < 0.7$; yellow: $0.5 < B_x < 0.6$; magenta: $0.4 < B_x < 0.5$; white: $B_x \leq 0.4$.



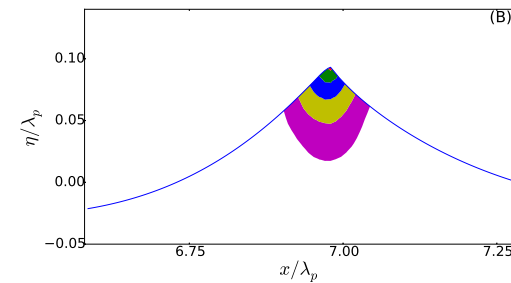
(a) Colour-coded zones of the breaking parameter B_x on the free surface at $t = 13.85$. The blue line is the location of the slice seen in 6c



(b) Colour-coded zones of the breaking parameter B_x on the free surface at $t = 14.41$. The blue line is the location of the slice seen in 6d



(c) Colour-coded cross-section within the slice $y = 0$ shown in figure 6a



(d) Colour-coded cross-section within the slice $y = 0$ shown in figure 6b

Figure 6: Contours of the breaking criterion B_x . The regions are colour-coded as follows: red: $B_x > 0.85$; green: $0.7 < B_x < 0.85$; blue: $0.6 < B_x < 0.7$; yellow: $0.5 < B_x < 0.6$; magenta: $0.4 < B_x < 0.5$; white: $B_x \leq 0.4$.

5. Conclusions and recommendations

A new criterion based on energy flux considerations is developed that detects the onset of breaking in 2D and 3D wave groups in deep and transitional water depths. The wave groups, generated by the WSIM Boundary Element Method code, show that the onset of breaking is a local effect superposed on the global wave motion. Depth-integrated quantities were not able to detect the signature of breaking generically in the phase-resolved wave motion. A more localised examination of the flow near the free surface is necessary to detect the initiation of breaking and to find a consistent deterministic indicator. Our new breaking criterion is based on the strength of the local energy flux relative to the local energy density, normalised by the local crest speed. This non-dimensional parameter, B which reduces to B_x at the crest maximum, simplifies remarkably at the free surface, reducing to a criterion for the ratio between the crest fluid speed to the crest speed. Extensive numerical experiments have shown that this new dynamical breaking onset parameter B possesses a threshold value, computed to be in the range [0.85, 0.86], above which any local crest will undergo breaking onset.

A detailed study of the geometry of the contours of B_x along the free surface and in depthwise slices of the fluid domain below shows that B_x reaches its maximum at the crest maximum on the free surface. A quantitative analysis indicates that the fluid domain where B_x first exceeds the breaking threshold has a horizontal extent on the free surface of $\approx 3\%$ of the wavelength.

Careful experiments are needed to validate these new findings. Such an experimental study is presently underway.

6. Acknowledgements

Funding for this investigation was provided by the Australian Research Council under Discovery Project DP120101701. Also, FD acknowledges partial support by the European Research Council (ERC) under the research project ERC-2011-AdG 290562-MULTIWAVE and Science Foundation Ireland under grant number SFI/12/ERC/E2227.

Appendix A. Depth-integrated energy flux exchange under very steep wave crests

This appendix provides details of the depth-integrated energy fluxes below steep crests in unsteady wave groups, and highlights our finding that depth-integrated quantities are unable to resolve very localised features such as the onset of breaking.

A.1. Energy distribution and depth-integrated energy fluxes in a wave group

In the accompanying figures 7a, 7b and 7c, all quantities are depth-integrated and made non-dimensional as described in 2. The top panel shows the spatial distributions of kinetic energy (KE), potential energy (PE) and total energy (TE). The second panel shows the modulus of the energy flux $F = \|\mathbf{F}\|$ and its horizontal component F_x . The last panel represents the corresponding horizontal gradient of the horizontal component ($-\partial F_x / \partial x$) of the energy flux. In these figures, the wave group travels towards the right and the x -axis represents position.

In these figures, panel 7a pertains to an evolving C3N5 wave packet shown at a moderately steep wave crest maximum that occurs early in the evolution towards its maximum recurrence. Panel 7b is the same C3N5 wave packet later in its evolution at its maximum recurrence and panel 7c is a marginally steeper C3N5 wave packet shown at the onset of breaking.

The top panel shows the energy ratios of a focusing group just prior to focus, and at focus. The potential energy is always dominant in crest regions, and the ratio PE/TE is close to 0.62, as described in detail in our companion paper Barthelemy *et al.* (2015). For each packet geometry investigated, the maximum energy level and growth rate at maximum focus both exceed, by a significant margin, the equivalent levels at maximum recurrence.

The second panel shows the similarity between the total energy flux F and its horizontal component F_x at the steepest wave crest. The total flux is horizontal at the crest and there are no differences between these two quantities. Quantitatively, the fluxes are higher when the group is focused. The maximum value of the net energy flow depends on the structure of the wave group, but for every case investigated, breaking crests have higher maximum values of the net energy flux than corresponding maximum recurrent wave crests.

However, the maximum values of the energies, the fluxes and the jump in the flux gradients cannot be used as a breaking discriminator. These values are ordered within a given wave group family, but not *between* the families. For example, we found that a recurrent case of the C3N9 family has a higher level of these values than a breaking case of the C3N5 family.

The gradients in the last panel exhibit a jump localised at the crest. The conservation relationship states

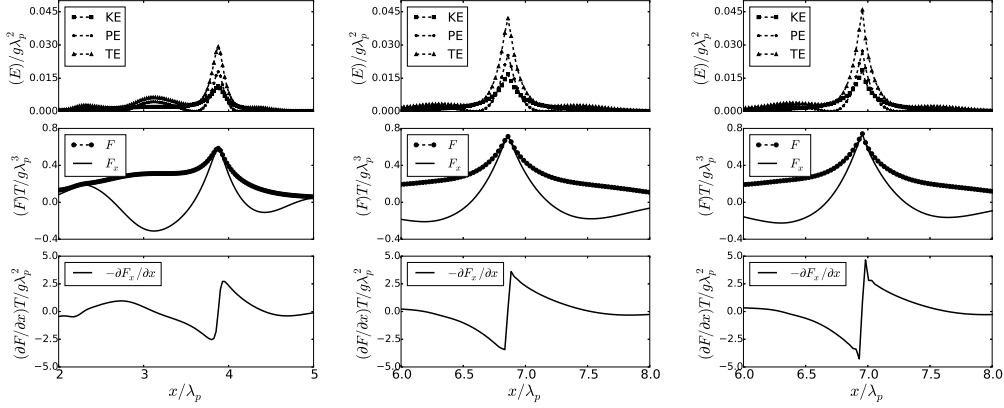
$$\frac{\partial}{\partial t} \int_{depth} Edz = -\frac{\partial}{\partial x_\alpha} \int_{depth} F_\alpha dz \quad (\text{A } 1)$$

and so a positive value of the right hand side implies net local energy growth. *A positive value on the right side of the figure means the wave is traveling towards the right.* In figure 7a, the jump in the gradient is asymmetric, with a higher value on the right side. The asymmetry implies the behaviour of the wavegroup, and a higher value on the positive side means that the group is focusing, and a lower value on the negative side of the jump means the group is defocusing, which is illustrated in figure 7a and figure 7b. The first wave group realisation is shown at a crest maximum, but the whole group will focus further as it evolves to the configuration shown in the second figure, which is at maximum recurrence, when the jump becomes symmetric. Beyond the recurrence maximum, defocusing begins, and the jump reverses with the negative side now higher than the positive side. In the breaking case, figure 7c, the jump maintains its focusing asymmetry.

A.2. Depth integrated energy flux budget over a variable-size integration box.

In this section the origin of the energy accumulation at the crest is investigated in more detail. The depth-integrated energy flux budget is computed over a variable-size box centered on the crest and also laterally relative to the crest. The following set of figures (Fig. 8) is computed for the same 2D wave group as seen in the preceding set of figures (Fig 7). The energy budget in the 2D wave group is computed along the wave propagation (x) direction. Two different plots are shown for each case. The first is the energy budget on a domain centered on the crest with a variable size Δx . The second is the budget computed on two different domains, $[-\Delta x, 0]$ and $[0, \Delta x]$, where the crest is one of the boundaries of the integration domain and is defined as zero. The symmetric budget is computed as follows, by the integration of the energy flux in the x direction:

$$\int_{-\Delta x}^{\Delta x} \left(-\frac{\partial F_x}{\partial x} \right) dx = F_x(-\Delta x) - F_x(\Delta x) \quad (\text{A } 2)$$



(a) Depth-integrated energies, energy fluxes and energy flux gradients of a C3N5A0.511 deep-water focusing wavegroup at crest maximum.

(b) Depth-integrated energies, energy fluxes and energy flux gradients of a C3N5A0.511 deep-water wavegroup at maximum recurrence.

(c) Depth-integrated energies, energy fluxes and energy flux gradients of a C3N5A0.514 deep-water wavegroup at the onset of marginal breaking.

Figure 7: Comparison between energies, energy fluxes and energy flux gradients

These budgets follow the sign convention for which a negative result implies a loss to the system and a positive result implies an input.

The three figures (8a, 8b and 8c) show that there is an energy input along the x -axis over a short spatial extent (20% of the wavelength for this crest maximum, and as the crest becomes steeper, around 8% for the maximum recurrence and the marginal breaking crests). The larger-scale budget result implies the crest is losing energy to its adjacent troughs as it evolves. The levels of energy exchange vary for each case. The crest maximum presented in the first panel (Fig 8a) reaches a maximum around 0.17 with a half-box size of around 0.12. The marginal recurrent crest (Fig 8b) has a maximum of around the same level as the first figure, but attains it with a half-box size of 0.04. The breaking crest reaches a maximum level of 0.38 with a half-box size of 0.04.

The bottom panels in the figure 8 show the energy budget on domains upstream or downstream of the crest. The top panels on a symmetric domain can be seen as the sum of the contributions from the $-\Delta x$ box and the $+\Delta x$ box. The bottom panels show the energy is growing upstream of the crest and decaying downstream of the crest. They also show that the maximum recurrence and the marginal breaking cases create almost the same amount of energy exchange but the net energy flux, their difference, is double for the marginal breaking case, as is seen in the top panel.

REFERENCES

ALLIS, MICHAEL 2013 The speed, breaking onset and energy dissipation of 3d deep-water waves. PhD thesis, Water Research Laboratory Faculty of Engineering UNSW.

BANNER, M. L., BARTHELEMY, X., FEDELE, F., ALLIS, M., BENETAZZO, A., DIAS, F. & PEIRSON, W. L. 2014 Linking reduced breaking crest speeds to unsteady nonlinear water wave group behavior. *Phys. Rev. Lett.* **112**, 114502.

BANNER, MICHAEL L. & PEIRSON, WILLIAM L. 2007 Wave breaking onset and strength for two-dimensional deep-water wave groups. *Journal of Fluid Mechanics* **585**, 93–115.

BANNER, MICHAEL L. & TIAN, XIN 1998 On the determination of the onset of breaking for modulating surface gravity water waves. *Journal of Fluid Mechanics* **367** (-1), 107–137.

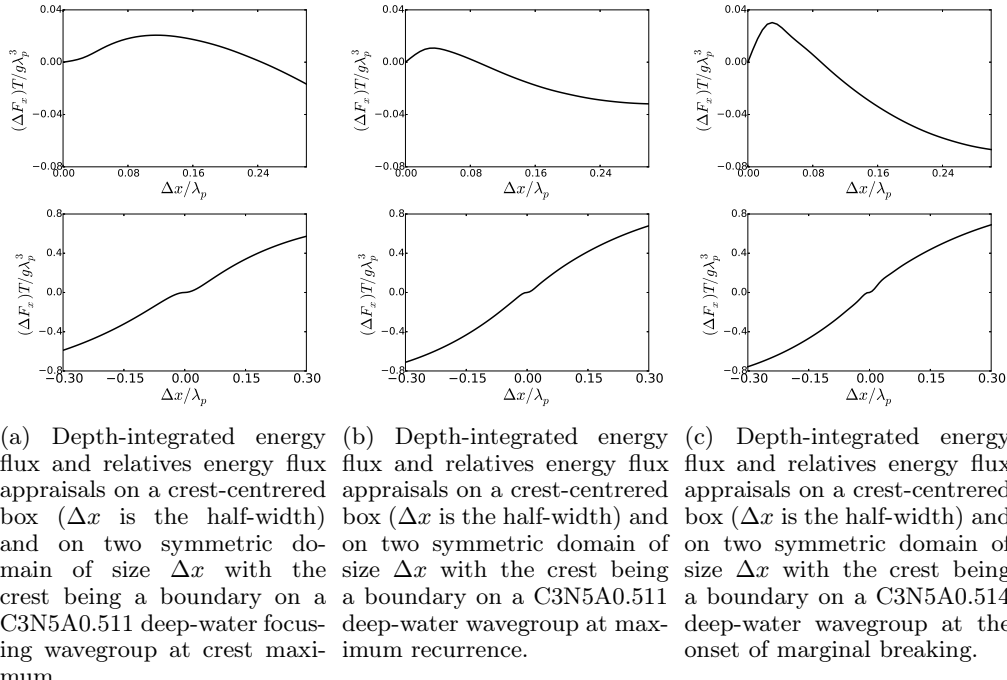


Figure 8: Appraisals of (relative) depth-integrated energy fluxes in a crest-centered box with ΔX the half width

BARTHELEMY, X., BANNER, M.L., PEIRSON, W.L., DIAS, F. & ALLIS, M. 2015 On the local properties of highly nonlinear unsteady gravity water waves. part 1. slowdown, kinematics and energetics. *Submitted to the Journal of Fluid Mechanics*.

CHALIKOV, DMITRY & BABANIN, ALEXANDER V. 2012 Simulation of wave breaking in one-dimensional spectral environment. *J. Phys. Oceanogr.* **42** (11), 1745–1761.

DALRYMPLE, R. A. 1989 Directional wavemaker theory with sidewall reflection. *Journal of Hydraulic Research* **27** (1), 23–34.

DALRYMPLE, ROBERT A. & KIRBY, JAMES T. 1988 Models for very wide-angle water waves and wave diffraction. *Journal of Fluid Mechanics Digital Archive* **192** (-1), 33–50.

GRILLI, STÉPHAN T. & HERRILLO, JUAN 1997 Numerical generation and absorption of fully nonlinear periodic waves. *Journal of Engineering Mechanics* **123** (10), 1060–1069.

GRILLI, S. T., SKOURUP, J. & SVENSEN, I. A. 1989 An efficient boundary element method for nonlinear water waves. *Engineering Analysis with Boundary Elements* **6** (2), 97 – 107.

KURNIA, R. & VAN GROESEN, E. 2014 High order hamiltonian water wave models with wave-breaking mechanism. *Coastal Engineering* **93** (0), 55 – 70.

LAMB, HORACE 1945 *Hydrodynamics*, 6th edn. New York: New York, Dover publications.

MA, QINGWEI. 2010 *Advances in numerical simulation of nonlinear water waves*. Hackensack, NJ: World Scientific.

PERLIN, MARC, CHOI, WOONYOUNG & TIAN, ZHIGANG 2013 Breaking waves in deep and intermediate waters. *Annual Review of Fluid Mechanics* **45** (1), 115–145.

PHILLIPS, OWEN 1977 *The dynamics of the upper ocean*, 2nd edn. Cambridge University Press Cambridge ; New York.

SCHULTZ, WILLIAM W., HUH, JIN & GRIFFIN, OWEN M. 1994 Potential energy in steep and breaking waves. *Journal of Fluid Mechanics* **278**, 201–228.

SHEMER, L. 2013 On kinematics of very steep waves. *Natural Hazards and Earth System Science* **13** (8), 2101–2107.

SONG, JIN-BAO & BANNER, MICHAEL L. 2002 On determining the onset and strength of breaking for deep water waves. part i: Unforced irrotational wave groups. *Journal of Physical Oceanography* **32** (9), 2541–2558.

STANSELL, PAUL & MACFARLANE, COLIN 2002 Experimental investigation of wave breaking criteria based on wave phase speeds. *Journal of Physical Oceanography* **32** (5), 1269–1283.

STOKES, G. G. 1847 On the theory of oscillatory waves. *Trans. Camb. Phil. Soc.* **8**, 441–455.

TIAN, ZHIGANG, PERLIN, MARC & CHOI, WOODYOUNG 2008 Evaluation of a deep-water wave breaking criterion. *Physics of Fluids* **20** (6), 066604.

TULIN, MARSHALL P. & LI, JIYUE J. 1992 On the breaking of energetic waves. *International Journal of Offshore and Polar Engineering* **2** (01).

WANG, PEI, YAO, YITAO & TULIN, MARSHALL P. 1993 Wave group evolution, wave deformation, and breaking: simulations using longtank, a numerical wave tank. In *The Third International Offshore and Polar Engineering Conference, 6-11 June, Singapore* (ed. International Society of Offshore & Polar Engineers), pp. –. International Society of Offshore and Polar Engineers.

WANG, PEI, YAO, YITAO & TULIN, MARSHALL P. 1995 An efficient numerical tank for non-linear water waves, based on the multi-subdomain approach with bem. *International Journal for Numerical Methods in Fluids* **20** (12), 1315–1336.